Combustion and Flame 160 (2013) 2251–2259

Contents lists available at SciVerse ScienceDirect

Combustion and Flame

journal homepage: www.elsevier.com/locate/combustflame

Effects of particle size and pressure on combustion of nano-aluminum particles and liquid water

Dilip Srinivas Sundaram [a], Vigor Yang [a,*], Ying Huang [b], Grant A. Risha [b], Richard A. Yetter [b]

[a] School of Aerospace Engineering, Georgia Institute of Technology, Atlanta, GA 30332, USA
[b] Department of Mechanical and Nuclear Engineering, The Pennsylvania State University, University Park, PA 16802, USA

ARTICLE INFO

Article history:
Received 4 March 2013
Received in revised form 28 April 2013
Accepted 28 April 2013
Available online 29 May 2013

Keywords:
Aluminum
Water
Combustion
Nano particles
Burning-rate
ALICE

ABSTRACT

The combustion wave propagation of nanoaluminum–water mixtures is studied theoretically and experimentally for particles in the size range of 38–130 nm and over a pressure range of 1–10 MPa. A multi-zone framework is established to predict the burning properties and flame structure by solving the conservation equations in each zone and enforcing the mass and energy continuities at the interfacial boundaries. The flame properties are measured by burning nanoaluminum–water strands in a constant-volume vessel. The present study deals with the downward propagating flame. Emphasis is placed on the effects of particle size and pressure. An analytical expression for the burning rate is derived, and physicochemical parameters that dictate the flame behavior are identified. For conditions present in the study, the burning rate shows pressure and particle size dependencies of the form r_b [cm/s] = $98.8 \times (p$ [MPa]$)^{0.32}(d_p$ [nm]$)^{-1.0}$. The flame thickness increases with increasing particle size and decreasing pressure. Results support the hypothesis that the combustion of aluminum–water mixtures is controlled by mass diffusion across the oxide layers of the particles.

1. Introduction

The combustion of aluminum particles in water is of relevance to many propulsion and energy-conversion applications. In metalized composite solid propellants, aluminum particles typically react with the combustion products of the polymeric binder and ammonium perchlorate, of which water vapor (H_2O) and carbon dioxide (CO_2) are two major species [1]. The problem is of particular interest for underwater propulsion, since the oxidizer (water) could be supplied from the environment [2]. The combustion of aluminum particles in water has also been studied in the contexts of hydrogen generation [3], nuclear reactor and industrial manufacturing safety [4], and underwater explosives [5]. The frozen mixture of aluminum particles and water (ALICE) is also under consideration for several energetic applications, due to its structural integrity [6,7].

The ignition and combustion characteristics of aluminum particles in water are different from those in oxygenated environments. Figure 1 shows the effect of pressure on the aluminum vaporization temperature ($T_{v,Al}$) and adiabatic flame temperature (T_f) of aluminum–water mixtures with different particle sizes and water in various thermodynamic states. The particles are assumed to be passivated, with an oxide shell thickness of 3 nm. The flame temperature is lower than the vaporization temperature for pressures over a "cut-off" value. For micron-sized particles, this occurs in the range of ~1–4 atm, depending on the thermodynamic state of water. For nano-sized particles, the cut-off pressure is as low as ~0.2 atm. This can be attributed to the fact that the inert oxide layer constitutes a greater portion of the particle mass at nanoscales; a 50 nm aluminum particle, for example, contains 32 wt.% oxide [5]. It should be pointed out that the actual flame temperature can be lower than the theoretical value, due to the effects of heat losses and incomplete combustion. As a result, in most practical cases, nano-aluminum does not vaporize and heterogeneous chemical reactions occur at the particle surface.

Figure 2 shows the effect of particle size on the ignition temperature of aluminum particles in water–vapor containing environments. Oxidation was studied by various methods including a thermogravimetric analyzer [8], electrical heating [9], shock tube [10], hydrogen–oxygen–argon burner [11], and arc burner [12]. Both spherical particles [8,10–12] and wire samples [9] were considered. In the thermo-gravimetric experiments [8], the particles were heated at relatively low rates in the range of 1–20 K/min. The oxidizing gas consisted of 27% H_2O and 73% Ar. The reactions were observed at much lower temperatures in water vapor than in oxygen. Specifically, a stepwise weight change was observed at the melting point of aluminum (660 °C) and the particle is completely oxidized at ~1000 °C. Note that the experimental conditions are different in the referenced studies. For example, the

* Corresponding author. Fax: +1 404 894 2760.
E-mail address: vigor.yang@aerospace.gatech.edu (V. Yang).

0010-2180/$ - see front matter © 2013 The Combustion Institute. Published by Elsevier Inc. All rights reserved.
http://dx.doi.org/10.1016/j.combustflame.2013.04.025

Nomenclature

C_p	specific heat
d_p	particle diameter
h_{fg}	enthalpy of water vaporization
k	velocity-to-thermal diffusivity ratio
M	mass
p	pressure
Q_r	heat of reaction
r	core radius
R	particle radius
r_b	burning rate
t	time
T	temperature
v	velocity
x	spatial coordinate
y	normalized spatial coordinate

Greek

ρ	density
δ_f	flame thickness
δ_v	water vapor zone thickness
α	thermal diffusivity
η	normalized particle diameter
θ	normalized temperature
κ	normalized burning rate
λ	thermal conductivity
μ	normalized heat release
τ_b	burning time
Φ	volume fraction

Subscript

0	reference/initial state
b	burn
f	flame, fluid
G	gaseous reaction zone
ign	ignition
lw	liquid water
m	mixture
ox	oxide
p	particle
u	unburned
V	water vapor zone
v	vaporization
W	liquid water zone
wv	water vapor

heating rates in shock tube experiments [10] are much higher ($\sim 10^6$ K/s) and the oxidizer concentration is different from those employed in other studies. It is also worthwhile to mention that the measured ignition temperature in burner [11,12] and shock tube [10] experiments corresponds to the temperature of the gas. The ignition temperature depends on various parameters such as the particle characteristics, oxidizer concentration, and heating rate. For these reasons, the referenced experimental data cannot be quantitatively compared directly. Nevertheless, it is true that the ignition temperature increases with increasing particle size in the range of 10 nm–100 μm. Even for larger particles, it remains lower than the melting point of the oxide layer, 2350 K. This suggests that the ignition temperatures of aluminum particles in water vapor are lower than those in oxygen. The phenomenon may be attributed to the stabilization of γ-oxide polymorph [8] and/or formation of a weaker hydroxide layer on the particle surface [9].

Many of the desirable traits of nano-sized particles are due to the presence of a large percentage of atoms on the surface [13]. The percentage of atoms on the surface layer of an aluminum

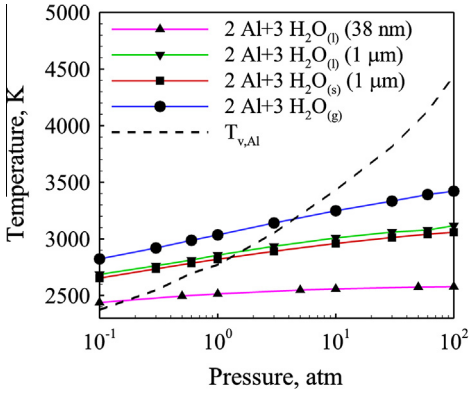

Fig. 1. Effect of pressure on aluminum vaporization temperature and adiabatic flame temperatures for various oxidizers.

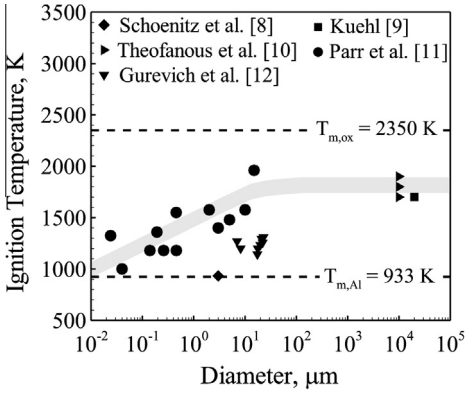

Fig. 2. Effect of particle size on ignition temperature of aluminum particles in water vapor.

particle increases from 2% to 92 %, when the particle size decreases from 100 to 1 nm [13]. The surface atoms have lower coordination numbers and higher energies than the atoms in the interior region of the particle. As a result, the thermophysical properties of nano-sized particles are significantly different from their corresponding bulk values. The melting temperature of nano-aluminum particles decreases from 933 to 473 K when the particle size decreases from 10 to 2 nm [14,15]. Similarly, the melting point of the oxide layer can be lower than the bulk value of 2350 K; for a shell thickness of 2.5 nm the melting point of the oxide layer is 1313 K [16]. The ignition temperatures and burning times of nano-aluminum particles are also lower than their micron-sized counterparts [17]. Significant enhancement in the burning characteristics is, thus, expected, when nano-sized particles are used to formulate energetic materials [18].

The combustion of nano-sized aluminum particles and water has been studied experimentally for a relatively wide range of pressure and particle size [5,19,20]. Results from earlier studies [19,20] suggested that the presence of a gelling agent such as polyacrylamide is necessary to achieve self-sustained deflagration.

Risha et al. [5,21], however, demonstrated self-deflagration of aluminum–water mixtures in a constant volume optical pressure vessel. The particle diameters covered a range of 38–130 nm and the pressure range of interest was 0.1–10 MPa. The measured burning rates were found to be inversely proportional to particle size and exhibited a pressure dependence of the form $r_b = ap^n$, with the exponent in the range of 0.27–0.47. Both transport and chemistry were speculated to affect the burning behavior, but key mechanisms and parameters are yet to be explored [5]. In the present study, a theoretical model is developed to study the flame propagation of a quasi-homogeneous mixture of nano-sized aluminum particles and liquid water. Special attention is placed on the effects of particle size and pressure on the flame structure and burning property. Results suggest that the combustion of nano-aluminum/water mixtures is controlled by mass diffusion through the oxide layer of the particles. Reasonably good agreement with experimental data is achieved, demonstrating the validity of the proposed model.

2. Experiment

The burning rates of nano-aluminum/water mixtures were obtained in an argon environment using a constant volume vessel, as shown schematically in Fig. 3. The chamber, made of stainless steel, is equipped with four optical viewing ports, each having a 15.2 × 2.54 cm field of view. The 61-cm long chamber has an inner diameter of 22 cm and a total free volume of 23 l; the relatively large volume minimizes the pressure variation caused by the generation of gaseous combustion products. The base plate has six feed-through ports to provide pathways for electrical signals and gas lines into the chamber. Nano-aluminum particles were obtained from Technology and Nanotechnology. They were mixed with stoichiometric amount of distilled water in a sealed plastic bag. Stoichiometry was calculated based on the active aluminum content in the particle. No gelling agent was employed. The mixture was then packed into a quartz glass tube (1 cm OD, 0.8 cm ID, 7.5 cm long). Ignition was achieved using a small ~1/8 in. thick propellant booster made of a homogenous double-base propellant (NOSOL 363) initiated by a resistance-heated nichrome wire threaded through the booster. The temporal evolution of the regressing luminous front was tracked and recorded using video equipment. Figure 4 shows captured images of stoichiometric mixture containing 80 nm particles burning at a pressure of 5.8 MPa. The flame front propagates through the packed mixture at a constant velocity. The measured position-time curve was used to determine the burning rate of the strand. More details of the experimental set-up can be found in [5].

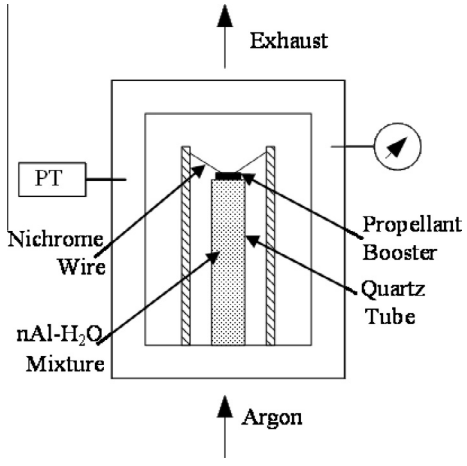

Fig. 3. Schematic of constant-pressure strand burner with optical access.

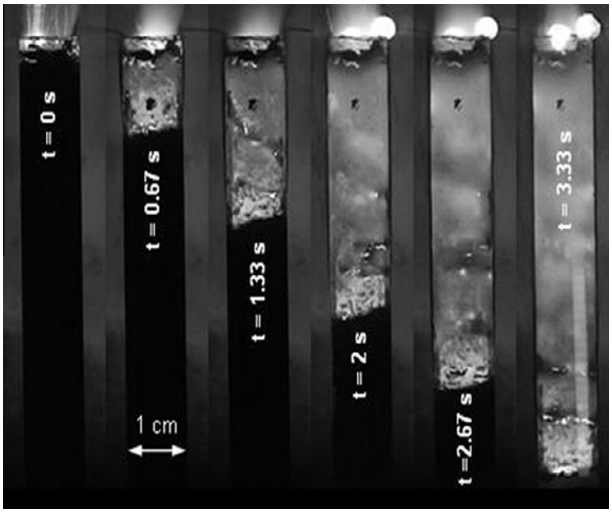

Fig. 4. Captured images of stoichiometric aluminum–water mixture containing 80 nm particles burning at a pressure of 5.8 MPa.

3. Theoretical framework

The analysis considers one-dimensional, isobaric, and planar flame propagation in a chemically reacting system consisting of passivated nano-aluminum particles and liquid water. Note that the present study deals with the downward propagating flame. For other conditions, the released hydrogen gas is likely to affect the heat transfer to the unburned mixture. The aluminum–water mixture is a viscous paste with dense particle loading and significant particle–particle interactions, as opposed to dust clouds that feature dilute particle concentrations [17,22]. Furthermore, the gaseous oxidizer (water vapor) is produced *in situ* by vaporization, instead of being supplied externally. The particles are assumed to be uniformly sized and their agglomeration is neglected. Flame propagation, which takes place through thermal conduction, is accompanied by a variety of physicochemical processes, including water vaporization, chemical reactions, and mass, momentum and energy exchanges between the fluid and particle phases. The system is approximated to be pseudo-homogenous, so that the particles and surrounding fluid are in thermal equilibrium locally. Water vaporization occurs on an infinitesimally thin plane. Figure 5 shows the multi-zone flame structure considered in the present study. The entire spatial domain is divided into three zones to demarcate the regions in which phase transition and chemical reactions occur. The initial temperature of the mixture is 298 K. Water undergoes a thermodynamic phase transition at the vaporization front, $x = -\delta_v$, where the local temperature reaches the vaporization point, T_v. The particles start to burn once the ignition temperature, T_{ign}, is attained. Chemical reactions are neglected in the preheat zones.

The thermal conductivity of the mixture, λ_m, depends on the loading density and thermal conductivity of the particles. The following correlation provides the best fit to experimental data for a wide range of particle volume fractions [23]:

$$\lambda_m = \lambda_p \exp\left(\frac{-1.5\Phi_f}{1-\Phi_f}\right), \tag{1}$$

where λ stands for the thermal conductivity and ϕ the volume fraction. The subscripts m, p, and f refer to mixture, particle, and fluid, respectively. Eq. (1) assumes that the fluid is non-conducting when

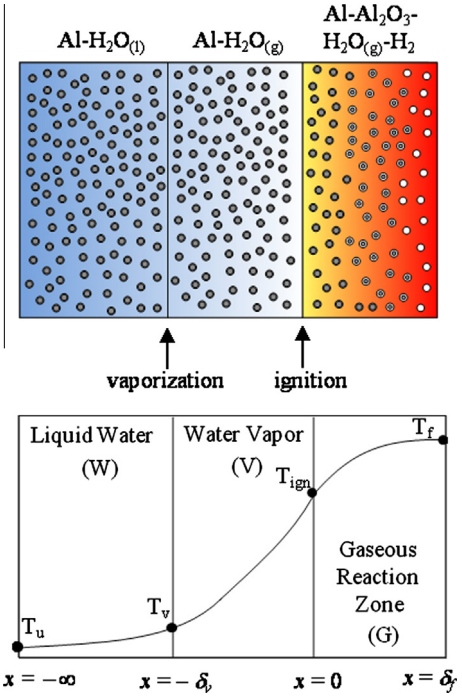

Fig. 5. Physical model and multi-zone flame structure (◯ Al, ◯ Al_2O_3).

compared with the particle. This is a reasonable approximation, since the former value is two or three orders of magnitude lower than the latter. Furthermore, it is reassuring to note that the thermal conductivity predicted by the correlation agrees with the experimental data for a wide range of particle volume fractions. The oxide layer hampers the flame propagation, due to its inefficiency as a conductor of heat. The overall thermal conductivity of the passivated aluminum particle, λ_p, is calculated as follows [24]:

$$\lambda_p = \frac{\lambda_{Al}^2 R}{(r-R)[2\lambda_{Al}\ln a - 2\lambda_{ox}\ln a - (\lambda_{Al}^2/\lambda_{ox})] + r\lambda_{Al}}, \tag{2}$$

where

$$a \equiv \frac{b-\lambda_{Al}R}{b-\lambda_{Al}(R-r)}; \quad b \equiv 2(R-r)\lambda_{ox} + 2r\lambda_{Al}. \tag{3}$$

Here r is the radius of the aluminum core and R the outer radius of the particle. The subscripts *Al* and *ox* refer to aluminum and oxide, respectively. The thermophysical properties of water and hydrogen are given in Refs. [25,26], while those of aluminum and its oxide are taken from Refs. [27–29], respectively. Table 1 summarizes the property data at a baseline pressure of 3.65 MPa. All properties are evaluated at an average temperature in each zone. The enthalpy of vaporization and boiling point of water are calculated as a function of pressure. A continuum-regime heat transfer model is considered, since the present study deals with pressures representative of those in practical propulsion systems. Free molecular effects are neglected without significant reduction in accuracy [6]. Mass and energy balances are enforced for a differential element in each zone. The resulting conservation equations are solved to obtain the burning rate and temperature distribution. The formulation is developed based on a coordinate system attached to the propagating flame.

3.1. Energy balance for the liquid water zone

The liquid water zone encompasses the region between the far field, $x = -\infty$, and the vaporization front, $x = -\delta_v$. The energy equation takes the form

$$(\rho_{Al}C_{p,Al}\Phi_{Al} + \rho_{ox}C_{p,ox}\Phi_{ox} + \rho_{lw}C_{p,lw}\Phi_{lw})r_b\frac{dT}{dx} = \lambda_{m,W}\frac{d^2T}{dx^2}, \tag{4}$$

subject to the boundary conditions:

$$T_{x\to-\infty} = T_u; \quad T_{x=-\delta_v} = T_v; \tag{5}$$

where ρ is the density, C_p the specific heat, r_b the burning rate, T the temperature, x the space coordinate, and δ_v the thickness of the vapor zone. The subscripts *W*, *u*, *v*, *ox*, and *lw* refer to the liquid water zone, unburned state, vaporization, oxide, and liquid water, respectively. An analytical solution to Eq. (4) is obtained for the temperature profile.

$$T = T_u + (T_v - T_u)\exp\{k_W(x+\delta_v)\}, \tag{6}$$

where k_W is the ratio of the burning rate to the thermal diffusivity, defined as

$$k_W = r_b/(\lambda_{m,W}/(\rho C_p)_W), \tag{7}$$

where (ρC_p) denotes the volume-averaged product of the density and specific heat of the mixture. The temperature profile depends on the burning rate and thickness of the water vapor zone, both of which are not known *a priori*.

3.2. Energy and mass balance for the water vapor zone

Water vapor generated at the vaporization front, $x = -\delta_v$, flows through the interstitial space between particles. The conservation of mass of water is enforced to determine the velocity of water vapor at the vaporization front

$$\rho_{lw}r_b = \rho_{wv}v_{wv}. \tag{8}$$

Here, v is the gas velocity. The subscript wv denotes water vapor. Eq. (8) can be used to express the energy equation in the following form:

$$(\rho_{Al}C_{p,Al}\Phi_{Al} + \rho_{ox}C_{p,ox}\Phi_{ox} + \rho_{lw}C_{p,wv}\Phi_{lw})r_b\frac{dT}{dx} = \lambda_{m,V}\frac{d^2T}{dx^2}, \tag{9}$$

subject to the interfacial conditions:

$$\begin{cases} x = -\delta_v : \lambda_m\frac{dT}{dx}\big|_V = \lambda_m\frac{dT}{dx}\big|_W + h_{fg}\Phi_{lw}\rho_{lw}r_b, \\ x = 0 : T = T_{ign}, \end{cases} \tag{10}$$

Table 1
Thermophysical properties of different species in three zones at baseline pressure of 3.65 MPa.*

Species	Thermal conductivity, W/m K			Specific heat, kJ/kg K			Density, kg/m^3		
	W	V	G	W	V	G	W	V	G
Aluminum	239	95	143	0.954	1.260	1.176		2700	
Aluminum oxide	22.20	9.50	6.40	0.930	1.200	1.303		4000	
Liquid water	0.70	–	–	4.400	–	–	995	–	–
Water vapor	–	0.07	0.12	–	2.330	2.580	–	8.58	5.17
Hydrogen	–	–	0.80	–	–	16.150	–	–	0.56

* T_v = 519 K, T_{ign} = 1360 K, T_f = 1800 K at p = 3.65 MPa W: liquid water zone; V: water vapor zone; G: gaseous reaction zone.

where h_{fg} is the enthalpy of water vaporization and T_{ign} the ignition temperature of nano-aluminum particles. The subscript V refers to the water vapor zone. The thickness of this zone is obtained by performing the heat-flux balance at $x = -\delta_v$:

$$\delta_v = \frac{1}{k_V}\log\left\{\left(1+\frac{\lambda_{m,V}k_V(T_{ign}-T_v)}{\lambda_{m,W}k_W(T_v-T_u)+h_{fg}\rho_{lw}\Phi_{lw}r_b}\right)\right\}. \tag{11}$$

The temperatures at the interfacial boundaries are matched to provide a closed-form solution to the energy equation:

$$T = \frac{1}{1-e^{-k_V\delta_v}}[T_v(1-e^{k_Vx}) - T_{ign}(e^{-k_V\delta_v}-e^{k_Vx})]. \tag{12}$$

3.3. Energy balance for the reaction zone

The stoichiometric reaction of aluminum particles with water vapor is given by

$$2Al + 3H_2O \rightarrow Al_2O_3 + 3H_2. \tag{13}$$

The properties are calculated by averaging their respective values of the reactant and product species. The energy equation can be expressed as [17]

$$\left(\sum_i \rho_i C_{p,i}\Phi_i\right) r_b\frac{dT}{dx} = \lambda_{m,G}\frac{d^2T}{dx^2} + \frac{\rho_m Q_r}{\tau_b}, \tag{14}$$

where Q_r is the chemical energy release per unit mass of the mixture, and τ_b the particle burning time. The subscripts G, m and i refer to the reaction zone, mixture, and species i, respectively. To facilitate the analysis, the temperature and spatial coordinate are normalized as follows:

$$\theta = \frac{T}{T_u}, \quad y = \frac{x}{r_b\tau_0}, \tag{15}$$

where τ_0 is the reference time scale defined as the particle burning time at a reference temperature. The location $y = 0$ is the ignition point of particles. Substituting the normalized variables defined in Eq. (15) into Eq. (14), the non-dimensional form of the energy equation is obtained

$$\frac{d^2\theta}{dy^2} - \kappa^2\frac{d\theta}{dy} = -\mu\kappa^2(\theta_{ign}-1)\frac{\tau_0}{\tau_b}. \tag{16}$$

Here $\kappa = r_b\cdot\sqrt{\tau_0/\alpha_{m,G}}$ is the normalized burning rate, with α being the thermal diffusivity. The normalized heat-release, μ, is written as

$$\mu = \frac{-\alpha_{m,G}\rho_m Q_r}{\lambda_{m,G}(T_{ign}-T_u)}. \tag{17}$$

The energy equation gives only a partial description of the underlying physicochemical phenomena in the reaction zone. In particular, an equation for the consumption of the particle mass is also needed.

3.4. Particle mass consumption in the reaction zone

The composition of the particle changes during the course of its reaction with water vapor. The aluminum content decreases progressively and a spherical oxide particle forms after complete oxidation. To characterize the combustion of individual particles, an equation for the particle mass consumption is considered

$$r_b\frac{dM_p}{dx} = -\frac{M_{p0}}{\tau_b}, \tag{18}$$

where M_p is the particle mass. The subscript *0* refers to the initial state. Eq. (18) can be re-written in terms of the particle size

$$\frac{d(d_p^3)}{dx} = -\frac{d_{p0}^3}{r_b.\tau_b}, \tag{19}$$

where d_p is the particle diameter. For consistency, the particle diameter is normalized as follows:

$$\eta = \frac{d_p}{d_{p0}}. \tag{20}$$

Substituting the normalized variable defined in Eq. (20) into Eq. (19), the non-dimensional form of the particle mass consumption equation is obtained

$$\frac{d\eta^3}{dy} = -\frac{\tau_0}{\tau_b}, \tag{21}$$

The following boundary conditions are specified to close the formulation:

$$\begin{cases} y = 0 : \lambda_m\frac{d\theta}{dy}\Big|_G = \lambda_m\frac{d\theta}{dy}\Big|_V, \quad \theta = \theta_{ign}, \quad \eta = 1 \\ y = 1 : \frac{d\theta}{dy} = 0, \quad \eta = 0. \end{cases} \tag{22}$$

The mass and energy balance equations in the reaction zone are solved numerically, with the burning rate treated as the eigenvalue. A shooting technique is employed to find the solution; the Newton–Raphson iteration method is used [30]. Numerical integration is achieved by means of the Rosenbrock method [30].

3.5. Heat release

The actual heat release from particle burning is lower than its theoretical counterpart due to incomplete combustion. The combustion efficiency of nano-aluminum/water mixtures is in the range of 80–100%, depending on the pressure and particle size [21]. Heat loss to the environment also occurs through thermal conduction and radiation. To incorporate these effects into the model, the normalized heat release is calculated based on the actual flame temperature. A simplified expression for the normalized heat release is obtained by integrating the energy equation, Eq. (16), and imposing the boundary conditions specified in Eq. (22)

$$\mu = \frac{\kappa^2(\theta_f-\theta_{ign}) + \frac{d\theta}{dy}\Big|_G}{(\theta_{ign}-1)}, \tag{23}$$

where the subscript f denotes the flame. Diakov et al. [31] studied the flame propagation of aluminum–water mixtures in a stainless steel chamber equipped with thermocouples at a pressure of 1 atm. The particle size is 100 nm and the oxide layer thickness is 1.84 nm. The measured flame temperature is 1800 K, which is significantly lower than the theoretical value of 2790 K for a particle size of 100 nm. The combustion efficiency is measured to be 87%. A similar scenario was observed for magnesium–water mixtures [32]. The combustion efficiency increases with decreasing particle size [21], although the adiabatic flame temperature is lower for smaller particles. For simplicity, a flame temperature of 1800 K is used to calculate the heat release for all particle sizes. Results of the sensitivity analysis indicate that the burning rate increases modestly with increasing flame temperature. At a pressure of 3.65 MPa and particle size of 38 nm, the burning rate increases from 5.59 to 6.85 cm/s when the flame temperature increases from 1800 to 2300 K.

3.6. Ignition temperature and burning time of particles

The present model requires, as input parameters, the ignition temperature and burning time of nano-aluminum particles. The ignition temperatures of Technanogy aluminum particles (24–192 nm) in water vapor vary between 1325 and 1360 K [11], as

shown in Fig. 2. For convenience, we assume the ignition temperature to be 1360 K.

The combustion of aluminum particles involves mass diffusion through the gas-phase mixture and oxide layer, and chemical reactions between the aluminum atoms and oxidizer molecules. For micron-sized and larger particles, combustion is controlled by species diffusion through the gas-phase product mixture; the burning time follows $d_p^{1.8}$-law and exhibits weak dependencies on temperature and pressure [17]. For particles smaller than 1 μm, the pressure and temperature of the ambient gas significantly influence the burning time [33], whereas the particle size exerts only a weak effect [17]. The latter trend may be attributed to the transition from the continuum to the free-molecular heat transfer regime [34] and/or sintering and agglomeration of particles. The present study deals with the conditions in the continuum regime, in which the burning time may be more size dependent. For nano-sized particles, surface tension leads to strong adherence of the oxide layer to the particle [35]. This phenomenon was also observed in molecular dynamics simulations [16].

The diffusion resistance provided by the oxide layer is several orders of magnitude greater than that of the gas-phase mixture. As a result, species diffusion through the oxide layer is the rate-controlling process [36]. Park et al. [37] studied the oxidation of nano-aluminum particles in air using single particle mass spectrometry for temperatures up to 1373 K. The measured oxidation rates exhibited reasonably good agreement with the results of the diffusion-controlled combustion model. The kinetically-controlled model, however, failed to capture the observed trends. These results support the hypothesis that the combustion of nano-sized aluminum particles is controlled by species diffusion processes rather than by chemical kinetics. To estimate the particle burning time, therefore, the diffusion coefficients of the reacting species in the oxide layer are required. They are, however, poorly known, and only with uncertainties of several orders of magnitude [38]. In the present study, the reaction time scale is approximated to be the particle burning time. This is physically justified because the energy release rate is dictated by the reactivity of the individual particles [17]. Theory suggests that the characteristic time scale for species diffusion through the oxide layer is inversely proportional to pressure and bears a d_p^2-relationship [36,37]. The observed particle size effect on the burning rate is obtained only if such a relationship is employed. A d_p^2-law is, thus, adopted for the burning time. The reference time scale is taken to be the burning time of a 24 nm aluminum particle and the pressure exponent in the burning time relationship varies between −0.3 and −1.0, depending on the ambient temperature [11,33]:

$$\tau_b = \frac{c[a_1 \exp(b_1 T) + a_2 \exp(b_2 T)] d_p^2}{p^m}, \tag{24}$$

$$m = a_3 \exp(b_3 T) + a_4 \exp(b_4 T), \tag{25}$$

where d_p is the particle diameter in nm and p the ambient pressure in atm. The constants are given in Table 3. The theoretical studies on oxidation of nano-aluminum particles also indicate that the diameter exponent in the burning time relationship is in the range 1.6–2.0 [38].

Table 2
Characteristics of aluminum particles.

Particle size, nm	Oxide layer thickness, nm	Al content, wt.%
38	3.10	54.3
50	2.10	68.0
80	2.70	75.0
130	2.20	84.0

Table 3
Constants in burning time expression.

Constant	Value
c	1.736×10^{-3}
a_1	204.650
b_1	-9.848×10^{-3}
a_2	1.842×10^{-4}
b_2	3.461×10^{-5}
a_3	7.075
b_3	-1.905×10^{-3}
a_4	4.023×10^{-1}
b_4	-3.120×10^{-4}

4. Analytical model of the mixture burning rate

With judicious simplifications, it is possible to obtain an analytical expression for the burning rate [32]. The specific heat capacities of different species and thermal conductivities of the mixture in the three zones (see Fig. 5) are assumed to be equal. The energy equation can be written as

$$[\rho_p(1-\Phi) + \rho_{lw}\Phi] C_p r_b \frac{dT}{dx} = \lambda \frac{d^2T}{dx^2}, \tag{26}$$

where Φ is the volume fraction of water. For an aluminum–water mixture, Φ takes the following form:

$$\Phi = \frac{\rho_p}{\rho_p + \rho_{lw}}. \tag{27}$$

Eqs. (11) and (12) are combined to provide an expression for the heat flux at $x = 0$ in the preheat zone

$$\lambda \left.\frac{dT}{dx}\right|_V = r_b \left[2 \frac{\rho_{lw}\rho_p}{\rho_{lw} + \rho_p} C_p (T_{ign} - T_u) + \frac{\rho_{lw}\rho_p}{\rho_{lw} + \rho_p} h_{fg} \right]. \tag{28}$$

The heat flux at $x = 0$ in the reaction zone is calculated by taking the spatial derivative of the analytical solution to Eq. (14)

$$\lambda \left.\frac{dT}{dx}\right|_G = \frac{\lambda Q_r}{\tau_b r_b C_p}, \tag{29}$$

By matching the two heat fluxes at $x = 0$, an analytical expression for the burning rate is obtained

$$r_b = \sqrt{\frac{\lambda}{\rho_m C_p} \cdot \frac{2Q_r}{2C_p(T_{ign} - T_u) + h_{fg}} \cdot \frac{1}{\tau_b}}, \tag{30}$$

where ρ_m is the density of the unburned mixture. The parameters that dictate flame propagation are the thermal diffusivity of the mixture, enthalpy of reaction, ignition temperature, and burning time. The inverse dependence of the burning rate on particle size implies diffusion-controlled combustion [5,39]. Eq. (30) resembles the Mallard-Le Chatelier formula [40] for the flame speed of a homogenous gas-phase mixture, except for the additional term accounting for the energy consumed to vaporize the water.

The obtained closed-form expression, Eq. (30), is used to estimate the burning rate of a stoichiometric aluminum–water mixture. The particle size and pressure are taken to be 38 nm and 3.65 MPa, respectively. The mean specific heat of the mixture is taken as 2.36 kJ/kg K. The thermal conductivity of the mixture in the reaction zone is calculated to be 1.21 W/m K. The density of the mixture is assumed to be equal to the theoretical value of 1800 kg/m^3. The enthalpies of reaction and vaporization of water are taken as 4400 and 1737 kJ/kg, respectively. The burning time is calculated as 0.07 ms. Substituting these values into Eq. (30), the burning rate is estimated to be 7.28 cm/s, which is within the range of 4.66–7.78 cm/s observed in the experiments [21]. The

obtained value is sensitive to changes in the burning time used in the model. For example, the burning rate increases from 7.28 to 8.6 cm/s, when the burning time decreases from 0.07 to 0.05 ms. The analysis demonstrates that the proposed model properly accounts for the underlying physicochemical processes. A more accurate result can be obtained by relaxing the simplifying assumptions.

5. Results and discussion

The theoretical framework described in Section 3 is employed to calculate the flame structure and burning rate of stoichiometric mixtures at different pressures and particle sizes. Table 2 shows the characteristics of the particles considered in the present study. The thickness of the oxide layer varies in the range of 2.10–3.10 nm. The active aluminum content decreases with decreasing particle size. The particle composition significantly influences the thermophysical properties of the mixture. As a result, it is important to use an appropriate value of the oxide layer thickness in the calculations. Figure 6 shows the temperature distribution for a stoichiometric mixture containing 38 nm aluminum particles at pressures of 1 and 10 MPa. The temperature increases from an initial value of 298 K in the preheat zone and attains a maximum value of 1800 K in the reaction zone. The thickness of the vapor and reaction zones decrease with increasing pressure. The temperature distribution is further altered by the fact that the vaporization temperature of water increases with pressure. An estimate of the reaction zone thickness is obtained by multiplying the flame propagation velocity and particle burning time. At a pressure of

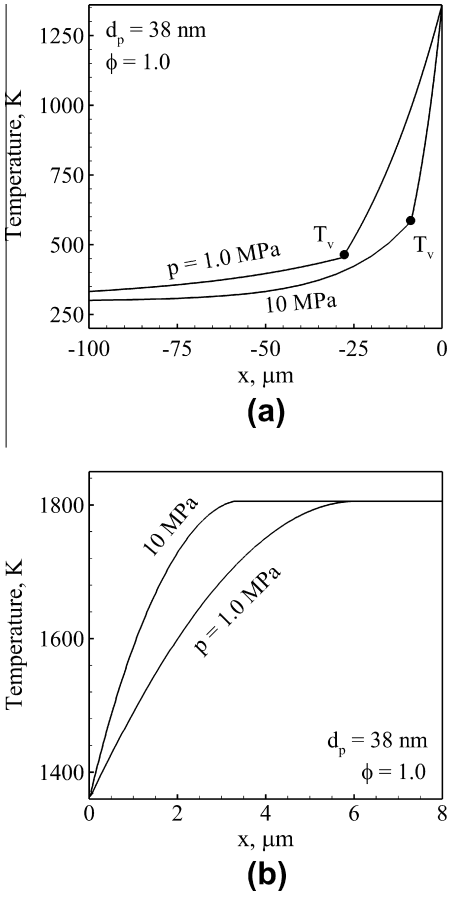

Fig. 6. Effect of pressure on temperature distribution of stoichiometric Al–H_2O mixture containing 38 nm particles in (a) the preheat zone; (b) the reaction zone.

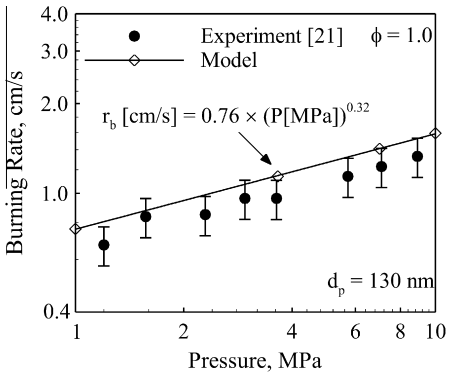

Fig. 7. Effect of pressure on burning rates of stoichiometric Al–H_2O mixtures containing 130 nm particles.

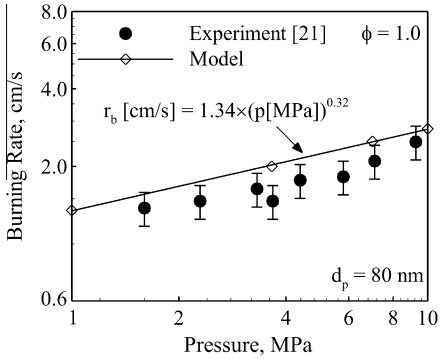

Fig. 8. Effect of pressure on burning rates of stoichiometric Al–H_2O mixtures containing 80 nm particles.

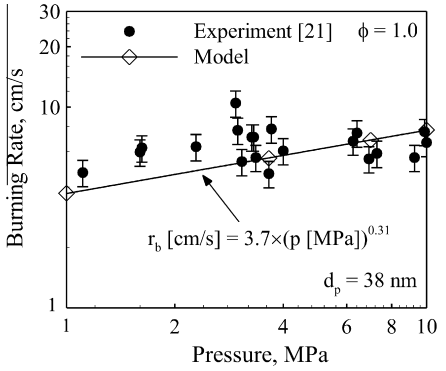

Fig. 9. Effect of pressure on burning rates of stoichiometric Al–H_2O mixture containing 38 nm particles.

1 MPa, the estimated value is 6 μm, which agrees reasonably well with the result of the present analysis.

Figures 7–9 show the effect of pressure on the burning rates for stoichiometric mixtures containing 130, 80, and 38 nm particles, respectively. For 130 nm particles, the burning rate increases from 0.76 to 1.59 cm/s when the pressure increases from 1 to 10 MPa. A similar trend is observed for the other two cases. For 38 nm particles, the presence of significant scatter in the burning rates can be attributed to the variations in the packing density of the mixture. The actual densities are in the range of 0.75–1.00 g/cm^3, which are lower than the theoretical value of 1.80 g/cm^3. Such a disparity is not observed for 80 and 130 nm particles, since fewer water

molecules are absorbed on the particle surface. The burning rate decreases with increasing packing density [21]. It is, thus, not surprising that some of the measured burning rates are greater than the predicted values. The pressure exponent in the burning rate law is ~0.3, which agrees reasonably well with experimental data. In a typical composite solid rocket propellant, the burning rate increases with increasing pressure. A general explanation for this phenomenon is that the flame stand-off distance decreases with increasing pressure, thereby increasing the heat flow to the propellant surface [41,42]. In the current study, a visible flame appeared to be attached to the burning surface, since the particles undergo heterogeneous surface reactions. The observed pressure effect can be attributed to the fact that the particle burning time decreases with increasing pressure.

Figure 10 shows the effect of particle size on the burning rate for a stoichiometric mixture at a pressure of 3.65 MPa. The burning rate shows a particle size dependence of $r_b = a \cdot d_p^n$, with an exponent of −1.15. The experimental data suggest that the burning rate is inversely proportional to the particle diameter [21]. In the present analysis, the particle burning time is assumed to follow d_p^2-law. The actual diameter exponent in the burning-time relationship may be slightly lower than 2, when simultaneous diffusion of water vapor and aluminum are considered [38]. This may explain the observed disparity between the predicted and measured values of the diameter exponent. Figure 11 shows a comparison of the measured and calculated burning rates with those obtained using the following correlation:

$$r_b\ [\mathrm{cm/s}] = 98.8 \times (p\ [\mathrm{MPa}])^{0.32} (d_p\ [\mathrm{nm}])^{-1.0}. \quad (31)$$

Reasonably good agreement is achieved, which demonstrates the validity of the correlation for situations encountered in the current study. The results support the theory that the rate-controlling mechanism is the mass diffusion through the oxide layers of the particles. In the present analysis, entrainment of particles in the gas flow has been neglected. The experiments indicate that a significant number of particles remained in the quartz tube instead of being transported out of the tube. This may be attributed to the inertial and gravitational forces, particle–particle interactions, and quartz tube wall effects. The region in which particle motion is likely to be important is the post-combustion zone, since the particles are under the continuous influence of the flow of the combustion gas (H_2). This can be incorporated into the model by considering the inertial and gravitational forces, interactions and collisions between particles, and confining effect of the quartz tube. The current model captures the main features of alumimum-water combustion, with reasonably good agreement between experimental data and model predictions.

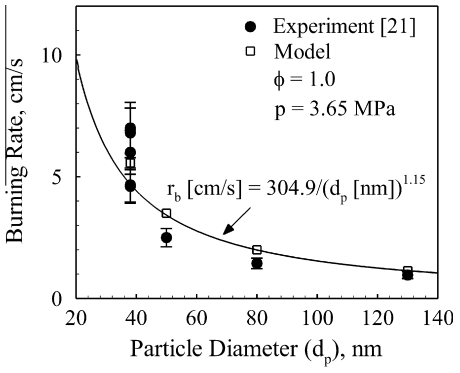

Fig. 10. Effect of particle size on burning rate of stoichiometric Al–H_2O mixture at 3.65 MPa.

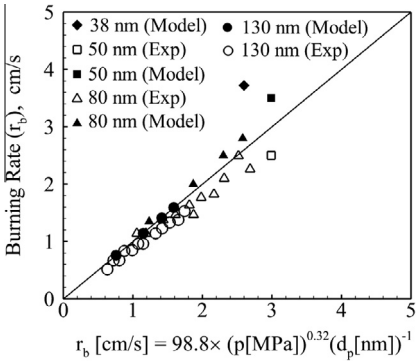

Fig. 11. Measured and calculated burning rates vs. curve-fit values for different particle sizes and pressures, $r_b\ [\mathrm{cm/s}] = 98.8 \times (p\ [\mathrm{MPa}])^{0.32} (d_p\ [\mathrm{nm}])^{-1.0}$.

6. Conclusions

The combustion wave propagation of nanoaluminum–water mixtures was studied theoretically and experimentally for particles in the size range of 38–130 nm and over a pressure range of 1–10 MPa. A multi-zone framework was established to predict the burning and flame properties by solving the conservation equations in each zone and imposing mass and energy continuities at the interfacial boundaries. The flame propagation characteristics were measured by burning nanoaluminum–water strands in a constant-volume vessel. Emphasis was placed on the effects of particle size and pressure. An analytical expression for the burning rate was derived, and physicochemical parameters that dictate the flame behavior were identified. For conditions present in the study, the burning rate showed pressure and particle size dependencies of $r_b\ [\mathrm{cm/s}] = 98.8 \times (p\ [\mathrm{MPa}])^{0.32} (d_p\ [\mathrm{nm}])^{-1.0}$. The flame thickness increased with increasing particle size and decreasing pressure. Results supported the hypothesis that the combustion of aluminum–water mixtures is controlled by mass diffusion across the oxide layers of the particles.

Acknowledgments

The authors would like to thank the Air Force Office of Scientific Research (AFOSR) and NASA for their sponsorship of this program under Contract No. FA9550-11-1-0002. The support and encouragement provided by Dr. Mitat Birkan is greatly appreciated.

References

[1] V. Yang, T.B. Brill, W.Z. Ren (Eds.), Solid Propellant Chemistry, Combustion, and Motor Interior Ballistics, AIAA Progress in Aeronautics and Astronautics, vol. 185, 2000, pp. 663–687.
[2] G.D. Roy (Ed.), Advances in Chemical Propulsion: Science to Technology, CRC Press, 2001 (chapter 8).
[3] E. Shafirovich, V. Diakov, A. Varma, Combust. Flame 144 (2006) 415–418.
[4] M. Epstein, H.K. Fauske, T.G. Theofanous, Nucl. Eng. Des. 201 (2000) 71–82.
[5] G.A. Risha, S.F. Son, R.A. Yetter, V. Yang, B.C. Tappan, Proc. Combust. Inst. 31 (2007) 2029–2036.
[6] D.S. Sundaram, V. Yang, T.L. Connell Jr., G.A. Risha, R.A. Yetter, Proc. Combust. Inst. 34 (2013) 2221–2228.
[7] G.A. Risha, T.L. Connell, Jr., D.S. Sundaram, R.A. Yetter, V. Yang. J. Prop. Power.
[8] M. Schoenitz, C.M. Chen, E.L. Dreizin, J. Phys. Chem. B 113 (2009) 5136–5140.
[9] D.K. Kuehl, AIAA J. 3 (1965) 2239–2247.
[10] T.G. Theofanous, X. Chen, P. Di Piazza, M. Epstein, H.F. Fauske, Phys. Fluids 6 (1994) 3513.
[11] T. Parr, C. Johnson, D. Hanson-Parr, K. Higa, K. Wilson, in: Proc. 39th JANNAF Combustion Subcommittee Meeting, Chemical Propulsion Information Agency, 2003.
[12] M.A. Gurevich, K.I. Lapkina, E.S. Ozerov, Fiz. Goreniya Vzryva 6 (1970) 172–175.
[13] D.S. Sundaram, P. Puri, V. Yang, Combust. Flame (2013), http://dx.doi.org/10.1016/j.combustflame.2013.03.031.
[14] P. Puri, V. Yang, J. Phys. Chem. C 111 (2007) 11776–11783.

[15] D.S. Sundaram, P. Puri, V. Yang, J. Phys. Chem. C 117 (2013) 7858–7869.
[16] P. Puri, V. Yang, J. Nanopart. Res. 12 (2010) 2989–3002.
[17] Y. Huang, G.A. Risha, V. Yang, R.A. Yetter, Combust. Flame 156 (2009) 5–13.
[18] R.A. Yetter, G.A. Risha, S.F. Son, Proc. Combust. Inst. 32 (2009) 1819–1838.
[19] V.G. Ivanov, S.N. Leonov, G.L. Savinov, O.V. Gavrilyuk, O.V. Glazkov, Combust. Explos. Shock Waves 30 (4) (1994) 569–570.
[20] V.G. Ivanov, O.V. Gavrilyuk, O.V. Glazkov, M.N. Safronov, Combust. Explos. Shock Waves 36 (2000) 213–219.
[21] G.A. Risha, J.L. Sabourin, V. Yang, R.A. Yetter, S.F. Son, B.C. Tappan, Combust. Sci. Technol. 180 (2008) 2127–2142.
[22] Y. Huang, G.A. Risha, V. Yang, R.A. Yetter, Proc. Combust. Inst. 31 (2007) 2001–2009.
[23] G. Tichá, W. Pabst, D.S. Smith, J. Mater. Sci. 40 (2005) 5045–5047.
[24] B. Badrinarayan, J.W. Barlow, Proc Solid Freeform Fabrication Symposium (1990) 91–97.
[25] E.W. Lemmon, M.L. Huber, M.O. McLinden, Reference Fluid Properties, National Institute of Standards and Technology, 2007.
[26] J.V. Sengers, J.T.R. Watson, J. Phys. Chem. Ref. Data 15 (1986) 1291–1314.
[27] W.F. Gale, T.C. Totemeier, Smithells Metals Reference Book, eighth ed., Elsevier, 2004.
[28] E.H. Buyco, F.E. Davis, J. Chem. Eng. Data 15 (1970) 518–523.
[29] R.G. Munro, J. Am. Ceram. Soc. 80 (1997) 1919–1928.
[30] W.H. Press, S.A. Teukolsky, W.T. Vetterling, B.P. Flannery, Numerical Recipes in Fortran, vol. 77, The Art of Scientific Computing, Cambridge University Press, 1992.
[31] V. Diakov, M. Diwan, E. Shafirovich, A. Varma, Chem. Eng. Sci. 62 (2007) 5586–5591.
[32] M. Diwan, D. Hanna, E. Shafirovich, A. Varma, Chem. Eng. Sci. 65 (2010) 80–87.
[33] T. Bazyn, H. Krier, N. Glumac, Combust. Flame 145 (2006) 703–713.
[34] C. Badiola, E.L. Dreizin, Proc. Combust. Inst. 34 (2013) 2237–2243.
[35] T. Bazyn, H. Krier, N. Glumac, Proc. Combust. Inst. 31 (2007) 2021–2028.
[36] O. Levenspiel, Chemical Reaction Engineering, John Wiley and Sons, New York, 1962. pp. 338–357.
[37] K. Park, D. Lee, A. Rai, D. Mukherjee, M.R. Zachariah, J. Phys. Chem. B 109 (2005) 7290–7299.
[38] A. Rai, K. Park, L. Zhuo, M.R. Zachariah, Combust. Theory Modell. 10 (2006) 843–859.
[39] R. Tomasi, Z.A. Munir, J. Am. Ceram. Soc. 82 (1999) 1985–1992.
[40] I. Glassman, R.A. Yetter, Combustion, forth ed., Academic Press, 2008.
[41] W. Cai, P. Thakre, V. Yang, Combust. Sci. Technol. 180 (2008) 2143–2169.
[42] M.W. Beckstead, K. Puduppakkam, P. Thakre, V. Yang, Prog. Energy Combust. Sci. 33 (2007) 497–551.